Gravitational signatures of lunar floor-fractured craters

Clément Thorey [*], Chloé Michaut, Mark Wieczorek

Institut de Physique du Globe de Paris, Sorbonne Paris Cité, Université Paris Diderot, CNRS, F-75013 Paris, France

A B S T R A C T

Lunar floor-fractured craters are impact craters characterized by distinctive shallow floors crossed by important networks of fractures. Different scenarios have been proposed to explain their formations but recent studies showed that the intrusion of magma at depth below the crater floor is the most plausible explanation. The intrusion of dense magma within the light upper-most part of the lunar crust should have left a positive signature in the gravity field. This study takes advantage of the unprecedented resolution of the lunar gravity field obtained from the NASA's Gravity Recovery and Interior Laboratory (GRAIL) mission, in combination with topographic data obtained from the Lunar Orbiter Laser Altimeter (LOLA) instrument, to investigate the gravitational signatures of both normal and floor-fractured craters. Despite the large variability in their gravitational signatures, the floor-fractured and normal craters in the Highlands show significant differences: the gravitational anomalies are significantly larger at floor-fractured craters. The anomaly amplitudes for floor-fractured craters are in agreement with synthetic gravity anomalies based on the predicted intrusion shapes from a theoretical flow model. Our results are consistent with magmatic intrusions intruding a crust characterized by a 12% porosity and where the intrusion has no porosity. Similar studies have been carried out in the lunar maria and South Pole–Aiken basin. Although the average gravitational signature of floor-fractured craters is larger than at normal craters in these regions, they cannot be distinguished statistically due to the small number of craters and the large variability of the anomalies. In general, a better characterization of the signal due solely to the initial impact crater is needed to isolate the magmatic intrusion signal and characterize the density contrast between the magma and crust.

© 2015 Elsevier B.V. All rights reserved.

1. Introduction

There are a class of impact craters on the Moon that are distinguished by having uplifted floors and radially/concentric floor-fractured networks. About 200 of these floor-fractured craters (FFCs) have been identified by Schultz (1976) and these impact craters are interpreted to have undergone endogenous deformations after their formation. The most striking feature of these craters is their shallow floors compared to normal craters of the same size, with the uplift reaching 50% of the initial crater depth in some cases (Schultz, 1976). Due to this deformation, their floors show large networks of radial, concentric and pentagonal fractures. Additionally, depending on local conditions, the uplift results in either a convex floor or a flat plate-like floor, sometimes with a wide circular moat just interior to the rim (Schultz, 1976; Jozwiak et al., 2012).

Intrusion of magma beneath the crater floor and viscous relaxation of the crater topography after the impact are two pro-posed scenarios to explain these deformations (Schultz, 1976; Hall et al., 1981; Wichman and Schultz, 1995; Dombard and Gillis, 2001). The recent theoretical model for the dynamics of crater-centered intrusions of Thorey and Michaut (2014) and recent morphological and geological studies by Jozwiak et al. (2012) showed that intrusion of magma beneath the crater floor is the most plausible scenario to produce the morphological features observed at floor-fractured craters.

Magmatic intrusions should be emplaced at their level of neutral buoyancy (Walker, 1989; Taisne and Tait, 2009; Wichman and Schultz, 1995). Upon cooling and solidification, however, their densities will be larger than the surrounding crustal material and hence, leave a positive signature in the gravity field. Schultz (1976) looked at the gravitational signature of some floor-fractured craters with gravity derived from radio tracking data acquired during the Apollo 15 and 16 missions (Sjogren et al., 1972, 1974). Except at the floor-fractured crater Taruntius, where a strong gravity anomaly was detected, no pronounced gravity anomalies were observed at other floor-fractured crater sites. However, the gravity data from these two experiments only covered a narrow swath along the equator and the resolution of the data used in these
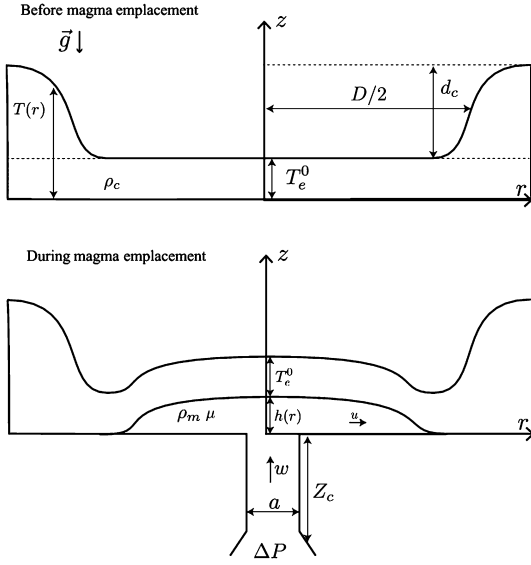
Fig. 1. Model geometry and parameters.

studies were not able to detect gravity anomalies for objects smaller than about 100 km in diameter (Schultz, 1976; Sjogren et al., 1974), which includes about 88% of the floor-fractured crater population.

Data from the NASA's Gravity Recovery and Interior Laboratory (GRAIL) mission have provided a global map of the Moon's gravity field with an unprecedented resolution. These data have been used to construct a model of the gravity field to spherical harmonic degree and order 900, which corresponds to a half-wavelength resolution of ~6 km at the lunar surface (Zuber et al., 2013; Konopliv et al., 2014). These data, used in combination with the topographic data obtained from the Lunar Orbiter Laser Altimeter (LOLA) instrument allow to investigate mass anomalies located in the lunar crust. In particular, these data allow to resolve small-scale density variations in the shallow crust (Besserer et al., 2014; Wieczorek et al., 2013) and they have been used to detect ancient igneous intrusions (Andrews-Hanna et al., 2013).

In this paper, after some theoretical considerations on the expected gravitational signal at floor-fractured craters in Section 2, we use GRAIL gravity to detect the presence of magmatic intrusions at floor-fractured crater sites in Section 3. Then, we develop a method to derive the density contrast between the magma and crust in Section 4. We discuss its geological implications in Section 5 and conclude in Section 6.

2. Theoretical considerations

The Bouguer anomaly associated with a magmatic intrusion beneath a crater depends upon the intrusion characteristics, namely its density and shape. Recently, we showed that the morphology of crater-centered intrusions depends mainly upon the thickness of the overlying elastic layer and on the crater size (Thorey and Michaut, 2014). Guided by the results and predictions of our model that is briefly summarized below, we here calculate and discuss the expected gravitational signal at floor-fractured crater sites.

2.1. Constitutive equations

In our model, the intrusion is fed at a constant rate through a cylindrical conduit located below the center of a crater floor and spreads horizontally along a thin bedding plane (Fig. 1). The magma makes room for itself by lifting the overlying assumed elastic layer, which is characterized by Young's modulus E, Poisson's ratio ν and an elastic thickness $T_e(r)$ given by

$$T_e(r) = T_e^0 + d_c \xi(r) \,, \text{ with } \xi(r) = \frac{1}{1 + e^{-\frac{2\alpha(2r-D)}{d_c}}} - \frac{1}{1 + e^{\frac{2\alpha D}{d_c}}} \tag{1}$$

where T_e^0 is the overlying layer thickness at the crater center, d_c the crater depth with respect to the pre-impact surface and $\xi(r)$ a normalized sigmoid function which reproduces a typical complex crater depression in terms of the crater diameter D and wall slope α (Fig. 1, top).

The thickness evolution equation in cylindrical coordinates for the flow of a Newtonian fluid is given by (Thorey and Michaut, 2014)

$$\frac{\partial h}{\partial t} = \frac{\rho_m g}{12\mu} \frac{1}{r} \frac{\partial}{\partial r} \left(rh^3 \frac{\partial h}{\partial r} \right) + \frac{\rho_c g \Psi T_e^0}{12\mu} \frac{1}{r} \frac{\partial}{\partial r} \left(rh^3 \frac{\partial \xi}{\partial r} \right)$$
$$+ \frac{E T_e^{0^3}}{144\mu(1-\nu^2)} \frac{1}{r} \frac{\partial}{\partial r} \left(rh^3 \frac{\partial}{\partial r} \left(\nabla_r^2 ((1+\Psi\xi)^3 \nabla_r^2 h) \right) \right)$$
$$+ w(r,t) \tag{2}$$

$$w(r,t) = \begin{cases} \frac{\Delta P}{4\mu Z_c}(\frac{a^2}{4} - r^2) & r \le \frac{a}{2} \\ 0 & r > \frac{a}{2} \end{cases} \tag{3}$$

where $h(r,t)$ is the intrusion thickness, r is the radial coordinate, t is time, ρ_m and ρ_c are the magma and crust density, μ is the viscosity, $\Psi = d_c/T_e^0$ is the thickening of the overlying layer at the wall, $w(r,t)$ is the injection velocity and $\Delta P/Z_c$ is the overpressure gradient driving magma ascent in the feeder dyke.

The terms on the right side of (2) respectively represent, from left to right, spreading due to magma weight, the lithostatic barrier the magma has to face at the crater wall, squeezing of the flow in response to elastic deformation of the overlying layer and injection rate. Eq. (2) is non-dimensionalized using the crater radius $D/2$ as a horizontal scale, a height scale H and a time scale τ given by

$$H = \left(\frac{12\mu Q_0}{\rho_m g \pi} \right)^{\frac{1}{4}} \tag{4}$$

$$\tau = \frac{\pi D^2 H}{4 Q_0} \tag{5}$$

where H is the characteristic height scale of a gravity current (Huppert, 1982) and τ is the characteristic time to fill up the crater depression for a constant injection rate

$$Q_0 = \frac{\pi \Delta P a^4}{128 \mu Z_c}. \tag{6}$$

Another useful lengthscale in the problem is the flexural wavelength Λ (Michaut, 2011)

$$\Lambda = \left(\frac{E T_e^{0^3}}{12(1-\nu^2)\rho_m g} \right)^{\frac{1}{4}} \tag{7}$$

which represents the wavelength of deformation of the elastic layer.

Eq. (2) made dimensionless becomes

$$\frac{\partial h}{\partial t} = \frac{1}{r} \frac{\partial}{\partial r} \left(rh^3 \frac{\partial h}{\partial r} \right) + \Xi \frac{1}{r} \frac{\partial}{\partial r} \left(rh^3 \frac{\partial \xi(r)}{\partial r} \right)$$
$$+ \Theta \frac{1}{r} \frac{\partial}{\partial r} \left(rh^3 \frac{\partial}{\partial r} \nabla_r^2 \left((1+\Psi\xi(r))^3 \nabla_r^2 h \right) \right)$$
$$+ \frac{32}{\gamma^2} \left(\frac{1}{4} - \frac{r^2}{\gamma^2} \right) \tag{8}$$

where $\xi(r)$ is also made dimensionless

$$\Theta = 10^{-2}$$
$$4\Lambda \sim D/2$$

Bell shaped intrusion

$$\Theta = 10^{-5}$$
$$4\Lambda << D/2$$

Cylinder-like intrusion

Bell shaped crater floor
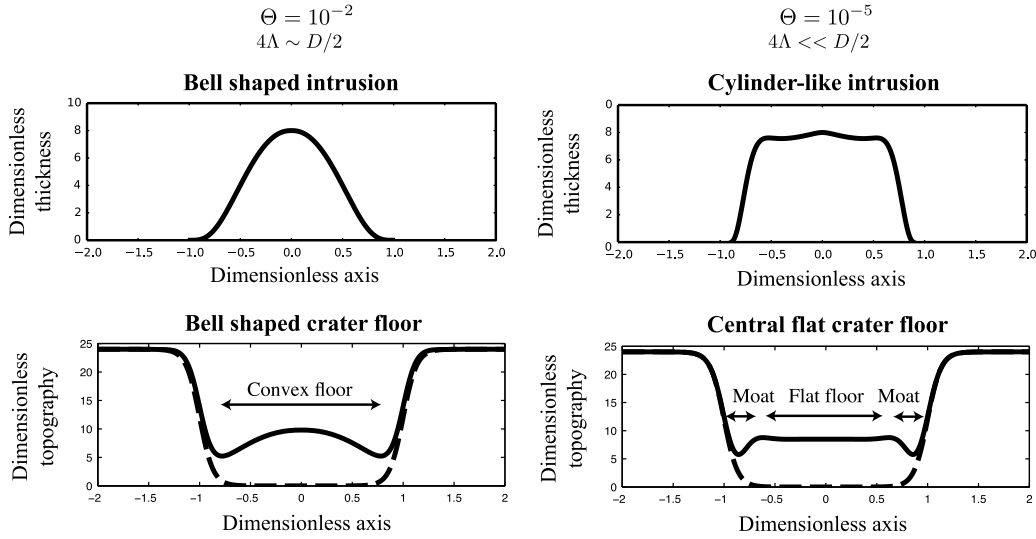
Central flat crater floor

Fig. 2. Two end-member intrusion shapes producing the two end-member floor deformations observed at FFC sites: convex floor (left) and plate-like floor (right).

$$\xi(r) = \frac{1}{1 + e^{-\frac{(r-1)}{\zeta}}} - \frac{1}{1 + e^{\frac{1}{\zeta}}} \quad (9)$$

and where

$$\gamma = \frac{2a}{D} = 0.02 \quad (10)$$

$$\zeta = \frac{d_c}{2\alpha D} = 0.13 \quad (11)$$

$$\Xi = \left(\frac{\rho_c g d_c}{\rho_m g H}\right) = 20 \quad (12)$$

$$\Psi = \frac{d_c}{T_e^0} = 1. \quad (13)$$

γ is the dimensionless source width, ζ is four times the normalized crater wall width and characterizes the crater geometry, Ξ is the ratio between the lithostatic pressure increase at the crater wall and the hydrostatic pressure due to a magma column of thickness H, which quantifies the importance of the lithostatic barrier at the crater wall, and Ψ is the dimensionless thickening of the upper elastic layer, which characterizes the elastic thickness increase at the crater wall. These are dimensionless parameters that do not significantly affect our results and are considered fixed in our analysis (Thorey and Michaut, 2014). The dimensionless number Θ

$$\Theta = \left(\frac{2\Lambda}{D}\right)^4 \quad (14)$$

is the dimensionless flexural wavelength of the upper layer raised to the power 4 that quantifies the length scale over which the elastic deformation is effective relative to the crater radius. It varies between 10^{-5} and 10^{-1} and has a strong influence on the intrusion shape and final floor appearance.

2.2. End-member modes of deformation

For a constant injection rate and no crater depression, i.e a constant upper elastic layer ($\xi(r) = 0$ and $T_e(r) = T_e^0$), the numerical resolution of the equations shows two spreading regimes (Michaut, 2011; Michaut et al., 2013). The flow is first driven by the bending of the upper elastic layer. The intrusion is bell-shaped and both the radius and the thickness evolve close to $t^{1/3}$.

When the radius becomes larger than 4Λ, the weight of the intrusion becomes dominant over the bending terms and the intrusion enters a gravity current regime. In this second regime, the intrusion shows a flat top with bent edges, the radius evolves as $t^{1/2}$ and the thickness tends to a constant (Huppert, 1982; Michaut, 2011).

For a constant injection rate and a crater-like topography for the upper layer, i.e. $T_e(r)$ given by (1), the spreading regimes are perturbed by the presence of the crater wall. The central flat floor of the crater first acts as a constant elastic upper layer and the intrusion spreads as described above. However, when it reaches the crater wall, the important increase in lithostatic pressure prevents the magma from spreading horizontally. The intrusion thickens in response and the crater floor is uplifted (Thorey and Michaut, 2014). Accordingly, the intrusion thickness can be estimated from the amount of uplift of the crater floor at the center.

The final morphology of the crater floor depends mainly on the ratio between the flexural wavelength and the crater radius, i.e. on the dimensionless number Θ (14). For a large value of Θ, i.e. a deep intrusion and/or a small crater, the intrusion reaches the wall in the bending regime. The intrusion is bell-shaped and the uplift of the crater floor leads to a shallowed convex floor (Fig. 2, left). In contrast, for a small value of Θ, i.e. a shallow intrusion and/or a large crater, the intrusion is in a gravity current regime when it reaches the crater wall. The thickening of the cylinder-like intrusion leads to a piston-like uplift of the crater floor and to a shallowed central flat floor for the crater (Fig. 2, right).

Accordingly, this model results into two main types of floor-fractured craters: craters with convex floors corresponding to bell-shaped intrusions (Fig. 2, left) and craters with plate-like floors corresponding to cylinder-shaped intrusions (Fig. 2, right). In the following, we consider craters of classes 2 and 4 of Schultz (1976) to represent manifestations of bell-shaped intrusions, and craters of classes 1, 3, 5 and 6 to be manifestations of cylinder-shaped intrusions.

2.3. Gravitational signature of FFCs: two case studies

The Bouguer gravity is the gravity anomaly that remains after taking into account the gravitational signature of surface topography. Thus, if there are no lateral variations in crustal density, the Bouguer anomaly of a floor-fractured crater should be entirely the result of the magmatic intrusion. The Bouguer anomaly associated
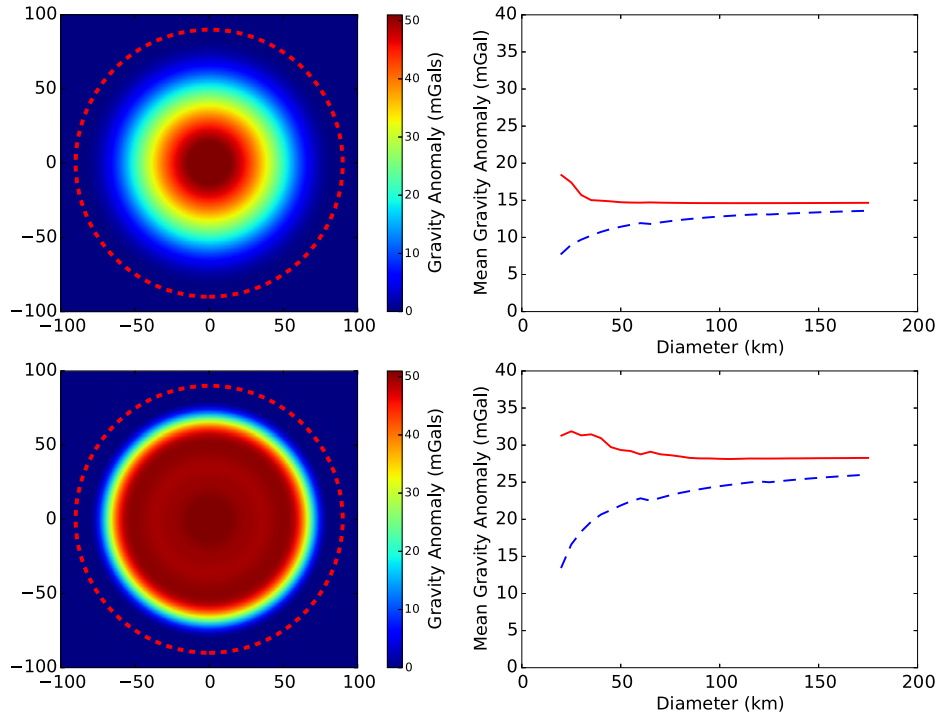
Fig. 3. Top left: Calculated synthetic gravity anomaly at $r = R_0$ for a bell-shaped intrusion located at the same elevation $R_m = R_0$ with $H_0 = 2$ km, $D = 180$ km and $\Delta\rho = 600$ kg m^{-3}. Dotted red line represents the crater rim. Top right: Mean synthetic gravity anomaly as a function of the crater diameter D for a bell-shaped intrusion with $H_0 = 2$ km and $\Delta\rho = 600$ kg m^{-3}. Red solid line: the intrusion is at the mean lunar radius $R_m = R_0$. Blue dashed line: the intrusion is 5 km below R_0, $R_m = R_0 - 5$ km. Bottom: Same as above, but for a cylinder-shaped intrusion. (For interpretation of the references to color in this figure legend, the reader is referred to the web version of this article.)

with a magmatic intrusion depends upon the intrusion morphology, the intrusion depth and the density contrast $\Delta\rho$ between the intrusion and the surrounding crust.

We investigate the signal expected at floor-fractured craters as a function of the intrusion shape, diameter and depth. In particular, for the bell and cylinder shaped intrusion, we study the signal for an intrusion diameter that varies between 20 and 180 km, i.e. the minimum and maximum diameter of floor-fractured craters observed by Schultz (1976) and two intrusion elevations R_m: at the mean lunar radius R_0 and at a reasonable maximum depth of 5 km below R_0 (Thorey and Michaut, 2014). We set the intrusion thickness H_0 to a value of 2 km, which is the maximum uplift observed by Schultz (1976) and the density contrast between the magma and the crust to a value of $\Delta\rho = 600$ kg m^{-3}, the maximum density contrast between mafic and crustal lunar rocks using the bulk densities of Kiefer et al. (2012).

The two end-member intrusion profiles are obtained by solving equation (8) for two different values of the dimensionless number Θ (14), $\Theta = 10^{-2}$ for the bell-shaped intrusion and $\Theta = 10^{-5}$ for the cylinder-like intrusion (Thorey and Michaut, 2014). We stop the simulations when the uplift at the center h_0 is significant and such that the pressure due to the intrusion weight at the center is about half the lithostatic pressure due to the crater wall ($h_0 = 10$). Finally, each profile is redimensionalized: the axial coordinate of the dimensionless thickness profile is multiplied by $D/2$ and the dimensionless thickness profile is multiplied by H_0/h_0, where h_0 is the dimensionless thickness of the intrusion at the end of the simulation.

We calculate the synthetic radial gravity anomaly (more precisely, the gravity disturbance) δ_g^s corresponding to each intrusion profile using the spherical harmonics expansion

$$\delta_g^s(r, \theta, \phi) = \frac{GM}{r^2} \sum_{l=0}^{L_{max}} \sum_{m=-l}^{l} \left(\frac{R_i}{r}\right)^l (l+1) C_{lm} Y_{lm}(\theta, \phi) \quad (15)$$

where r, θ and ϕ are the coordinates of observation, G is the gravitational constant, M the mass of the Moon, R_i the reference radius of the spherical harmonic coefficients taken as the mean elevation at the site of intrusion, i.e. $R_i = R_m + \bar{h}$ where $\bar{h}$ is the mean intrusion thickness, C_{lm}, and Y_{lm} the spherical harmonic functions of degree l and order m (Wieczorek and Phillips, 1998). Gravitational accelerations are considered positive when directed downward (see Supplementary materials for the expression of the spherical harmonic coefficients associated with the intrusion thickness profile and the calculation details).

The two different intrusion shapes result in two different types of anomaly (Fig. 3, left). For a bell-shaped intrusion, with a convex crater floor, the gravity anomaly is also bell-shaped. It decreases gradually from the center to the crater wall (Fig. 3, top left). For an intrusion placed at $R_m = R_0$, the signal barely depends on the crater diameter. The mean gravity anomaly measured interior to the crater wall is almost constant and about 15 mGal (Fig. 3, top right). Although an increased intrusion depth decreases the mean value of the anomaly by a factor that is less than two for craters smaller than 50 km, it barely affects the anomaly for craters larger than 50 km (Fig. 3; top right).

For a cylinder-like intrusion and a plate-like crater floor, the gravity anomaly is relatively uniform and sharply decreases at the crater wall (Fig. 3, bottom left). Consequently, although the maximum amplitude of the anomaly is similar to the one produced by a bell-shaped intrusion, the mean gravity anomaly, measured interior to the crater wall, is twice larger and about 30 mGal. Similar to bell-shaped intrusion, an increased intrusion depth decreases the mean value of the anomaly by a factor that is less than two for craters smaller than 50 km but barely affects the anomaly for craters larger than 50 km (Fig. 3, bottom right).

One important observation of our modeling is that even for an extreme case of a 2 km thick and a 180 km diameter intrusion placed at the surface with a large density contrast of 600 kg m^{-3},

the expected signal is only of a few tens of mGal. Though GRAIL can easily detect such small amplitude anomalies, this gravity signals could be masked by both large-scale regional signals and short-wavelength signals that are unrelated to our idealized model of Fig. 1. Therefore, we need to filter out these other contributions to be able to detect the potential presence of magmatic intrusions at floor-fractured craters. In the following, we present the gravity model that we use and consider the remaining expected signal after filtering the synthetics the same way the observed gravity are filtered.

2.4. Filtered GRAIL gravity

The observed gravity field on the Moon is a result of several contributions, including surface topography, relief along the crust–mantle interface and density heterogeneities in both the mantle and the crust. In order to detect the presence of magmatic intrusions in the shallow crust, which have predicted anomalies of only a few tens of mGal, we first remove all known signatures from the observed gravity field in order to highlight those signals that remain.

To construct this model, we start with JGGRAIL 900C11A gravity field, which is developed to spherical harmonic degree 900 and which is based on all data obtained during the GRAIL primary and extended mission (Konopliv et al., 2014). From the free-air gravity model, we first compute the Bouguer anomaly by removing the gravitational contribution of surface topography and the long-wavelength variations in crustal density that are predicted from remote sensing data, as described in Wieczorek et al. (2013). The most prominent signals that remain are either associated with large impact basins or are anticorrelated with long-wavelength topography. We interpret the majority of this signal as being the result of crustal thickness variations, and use the Bouguer anomaly to invert for the gravitational signal of relief along the crust–mantle interface, as described in Wieczorek et al. (2013).

Since the shortest wavelength signals in the Bouguer anomaly are unlikely to be the result of crustal thickness variations, and since short-wavelength signals become highly amplified when extrapolated with depth below the surface, we apply the low-pass filter of Wieczorek and Phillips (1998) to the Bouguer anomaly before inverting for crustal thickness variations. This filter is parameterized by having a value of 0.5 at spherical harmonic degree λ. The choice of λ is subjective, and λ is chosen such that the obtained crustal thickness map does not contain excessive power at the shortest wavelengths. In Wieczorek et al. (2013), λ was chosen to have a value of 80. Here, we test several values for λ and find that $\lambda = 80$ is also a good trade-off between the removal of regional trends and the removal of signals due to the magmatic intrusion itself (see Supplementary Fig. 1 for details on the effects of λ).

After removing the gravitational signal of the crustal–mantle interface from the Bouguer anomaly, the remainder of the signal is attributed to lateral variations in density within the crust of the Moon. To remove short wavelength noise in the gravitational field, we also apply a cosine filter to the spherical harmonic coefficients between degree 550 and 650. It is from this map, here referred to as CrustAnom, that we search for gravitational anomalies associated with floor-fractured craters. Our model CrustAnom is roughly equivalent to a band-passed Bouguer anomaly, where both the shortest and longest wavelength signals are removed (Fig. 4).

Upon applying the same filtering to synthetic gravity anomalies, the expected signal at floor-fractured craters is reduced with respect to those considered in Section 2.3 (Fig. 5). The filtering, which affects mostly large craters, leads to a drop in the amplitude of the gravity anomaly by a factor larger than two for craters larger than about 80 km. As an example, the mean anomaly for the
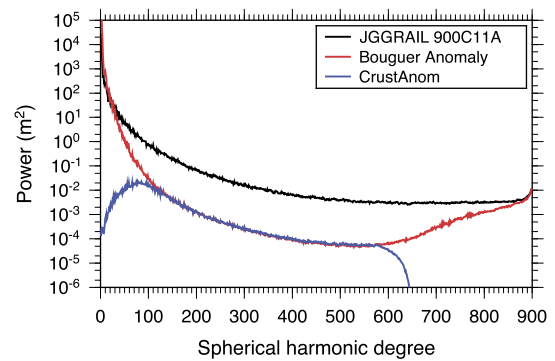

Fig. 4. Power spectra for various gravity models. Black solid line: free-air gravity from the GRAIL gravity model JGGRAIL 900C11A. Red solid line: Bouguer gravity anomaly assuming a constant crustal density of 2550 kg m^{-3}. Blue solid line: Crustal gravity anomaly of our model CrustAnom with $\lambda = 80$ and which removes long-wavelength variations in crustal density as predicted by remote sensing data. (For interpretation of the references to color in this figure legend, the reader is referred to the web version of this article.)

extreme case of a 2 km thick and 180 km large intrusion should only be of a few mGal in the model CrustAnom (Fig. 5).

3. Gravitational signature of lunar craters

The gravitational signal associated with magmatic intrusions at floor-fractured craters will be superimposed on the signal of a normal impact crater. We use the model CrustAnom to first quantify the gravity signal at normal impact craters and then compare to the signal at floor-fractured craters.

3.1. Normal and floor-fractured crater populations

We use the dataset of Head et al. (2010) as a reference catalog for normal craters and the dataset of Jozwiak et al. (2012) as a reference catalog for floor-fractured craters. We consider only complex craters and thus use a minimum crater diameter of 20 km, which is the transitional crater diameter between simple and complex lunar craters (Pike, 1974, 1980). We use a maximum crater diameter of 180 km, because for larger craters, the mantle uplift associated with basin formation becomes apparent in the gravity data (Melosh et al., 2013). These criteria result in a population of 116 floor-fractured and 5101 normal craters covering the whole lunar surface.

The observed gravity field of an impact crater will depend upon the density of the crust. GRAIL gravity data show that crustal density is not constant, and that regional variations of ± 250 kg m^{-3} exist, primarily between the highlands and the South Pole–Aitken basin (SPA). In addition, surface densities in the maria are considerably higher than in the highlands (Besserer et al., 2014). To minimize potential biases that might arise from regional variations in crustal density or geologic evolution, we divide each crater population (normal and floor-fractured craters) into three sub-populations. The first is constituted by craters that lie within the highlands, outside of both the maria and South Pole–Aitken basin. We use the USGS geological maps to define the mare borders and the SPA basin is defined using the best-fit outer ellipse of Garrick-Bethell and Zuber (2009). In the highlands, there are 80 floor-fractured and 4054 normal craters (Fig. 6, top left). The second sub-population is constituted by craters that lie within the maria and outside of SPA basin of which there are 22 floor-fractured and 306 normal craters (Fig. 6, middle left). The last sub-population is constituted by craters within the SPA of which there are 14 floor-fractured and 603 normal craters (Fig. 6, bottom left).

In each region defined above, the spatial distribution of floor-fractured and normal craters is different (Fig. 6, left). To minimize
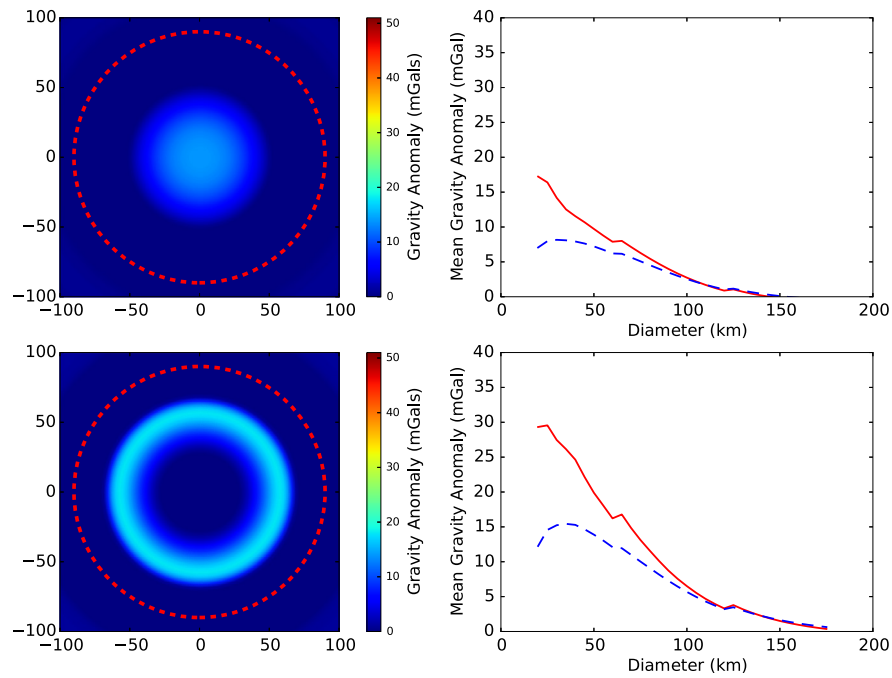
Fig. 5. Top left: Calculated synthetic gravity anomaly at $r = R_0$ filtered the same way as the model CrustAnom for a bell-shaped intrusion at the same elevation $R_m = R_0$ with $H_0 = 2$ km, $D = 180$ km and $\Delta\rho = 600$ kg m^{-3}. Dotted red line represents the crater rim. Top right: Mean filtered synthetic gravity anomaly as a function of the crater diameter D for a bell-shaped intrusion with $H_0 = 2$ km and $\Delta\rho = 600$ kg m^{-3}. Red solid line: the intrusion is at the mean lunar radius $R_m = R_0$. Blue dashed line: the intrusion is 5 km below R_0, $R_m = R_0 - 5$ km. Bottom: Same as above, but for a cylinder-shaped intrusion. (For interpretation of the references to color in this figure legend, the reader is referred to the web version of this article.)
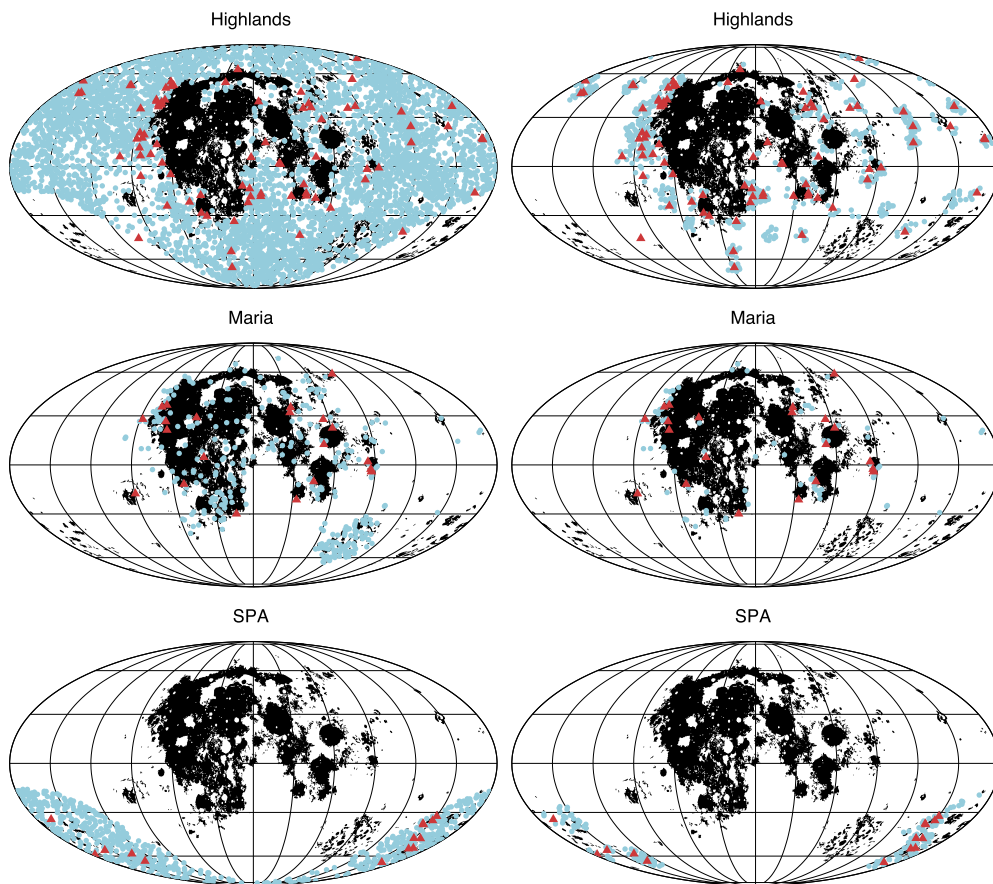

Fig. 6. (Top row) Left: All FFCs (red triangles) and normal craters (light blue circles) in the highlands. Right: All FFCs (red triangles) and normal craters that have the same spatial distribution as the FFCs (light blue circles). **(Middle row)** Same plots but for craters in the maria. **(Bottom row)** Same plots but for craters in South Pole–Aitken basin (SPA). (For interpretation of the references to color in this figure legend, the reader is referred to the web version of this article.)
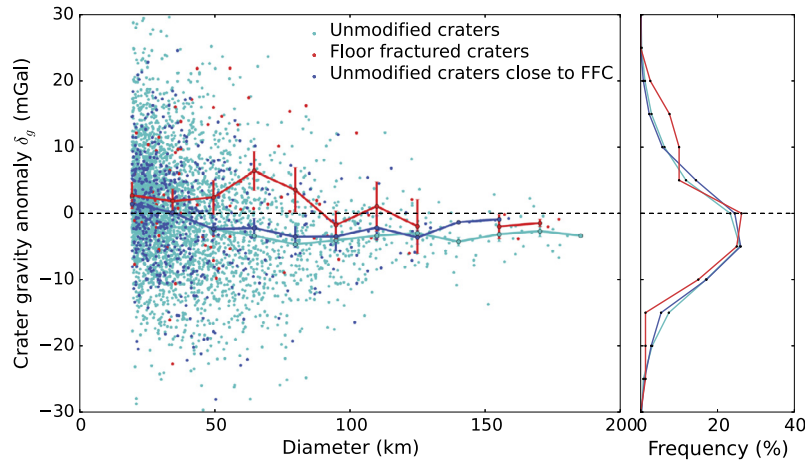
Fig. 7. Magnitude of the gravity anomaly δ_g versus diameter D for the normal crater population (light blue dots), the normal crater population that shares the FFC spatial distribution (blue dots) and the floor-fractured crater population (red dots) in the highlands. Solid line: Mean of the gravity anomalies binned in 15 km diameter intervals. Error bars correspond to the standard error for each bin. Right plot: Corresponding gravity anomaly density distribution for each population in frequency (%). (For interpretation of the references to color in this figure legend, the reader is referred to the web version of this article.)

any biases that might result from different regional characteristics, we also consider, for each region, a second sub-population of normal craters that shares the same spatial distribution as floor-fractured craters (Fig. 6, right). In this sub-population, we consider all normal craters that are less than 150 km away from a floor-fractured crater.

3.2. Crater gravitational signatures

In analyzing the gravitational signature of lunar impact craters, we make use of a single number, the crater gravity anomaly, that is defined as the average gravitational anomaly with respect to the regional value. In calculating this number, we first calculate the average gravitational anomaly from our model CrustAnom within the main crater rim, i.e. within a circular region defined by its radius $D/2$ where D is the crater diameter reported by Head et al. (2010) and Jozwiak et al. (2012). We then subtract from this value the average value of the gravity field in an annulus extending from the crater rim to a radius of one crater diameter D (Supplementary Fig. 2). Both gravitational anomalies are calculated at the average elevation of the crater.

3.2.1. Highlands

The magnitude of the gravity anomalies at normal crater sites shows an important variability (Fig. 7). On average, the anomaly is positive at the smallest craters, slowly decreases with increasing diameters, and approaches a constant negative value near a diameter of about 100 km. For crater diameters between 100 and 180 km, the mean magnitude of the gravity anomalies is independent of the diameter and close to −5 mGal. The mean of the gravity anomalies for the whole population μ_{δ_g} is negative and equal to −0.71 mGal. This number is well constrained due to the large number of craters. In particular, the uncertainty in the mean (the standard error, which is the standard deviation divided by the square root of the number of observations) is equal to 0.12 mGal. The population that shares the spatial distribution of floor-fractured craters shows similar trends (Fig. 7). A Kolmogorov–Smirnov (KS) test was conducted to compare this population to the whole population of normal craters. The test reports a value of p, which is the probability that the two population are drawn from the same distribution, larger than 10%, which confirms that no significant differences exist between the two populations (Supplementary Table 1).

The magnitude of the gravity anomalies at floor-fractured craters shows a different dependence with diameter than at nor-

mal craters (Fig. 7). Although the variance of the data with respect to the average is of the same order, the gravity anomalies at floor-fractured craters are larger. In particular, the mean of the floor-fractured crater gravity anomalies is positive and approximately 2.7 mGal larger than the mean of the normal crater gravity anomalies. We made use of a t-test to determine the robustness of the difference between the mean magnitude of the gravity anomalies of the two populations. This test quantifies the significance of a difference between the means of two populations assuming the two populations have the same variance. We found that there was only less than a 5% chance that the difference in the mean of the two populations could have occurred by chance (Supplementary Table 1). The same result holds for the comparison with the normal crater population that shares the spatial distribution of floor-fractured craters (Supplementary Table 1).

3.2.2. Lunar maria and SPA

The magnitude of the gravity anomalies at the sites of complex craters in the lunar maria shows a variability that is similar to craters in the highlands (Fig. 8, top). The gravity anomaly remains close to 0 mGal and is independent of the crater diameter (Fig. 8, top). The mean of the whole population μ_{δ_g} is positive and equal to 1.51 ± 0.68 mGal. A KS test shows that there is no significant difference between the entire normal crater population and the one that shares the spatial distribution of floor-fractured craters (Fig. 8, top, Supplementary Table 1).

The normal craters in the South Pole–Aikten basin show gravity anomalies that are somewhat more negative than in the highlands (Fig. 8, bottom). On average, the signal decreases with increasing diameter up to $D \sim 100$–120 km (Fig. 8, bottom) and increases somewhat again for crater diameters between 120 and 180 km (Fig. 8, bottom). A KS test shows that there is no significant difference between the two populations of normal craters (Fig. 8, bottom, Supplementary Table 1).

Although the mean magnitude of the gravity anomalies at FFC sites is about 3 mGal larger than the mean value observed at normal craters in the maria and SPA, the variability in the signal is large and there is no significant statistical difference between the mean of the gravity anomalies of normal and floor-fractured craters in those two different regions. Indeed, a t-test, realized for both regions, shows that there was more than a 10% chance that these differences in the mean of the two populations could have occurred by chance (Supplementary Table 1). Nevertheless, the small number of FFCs in the maria and in the SPA makes difficult to obtain a significant statistic due to the low accuracy in
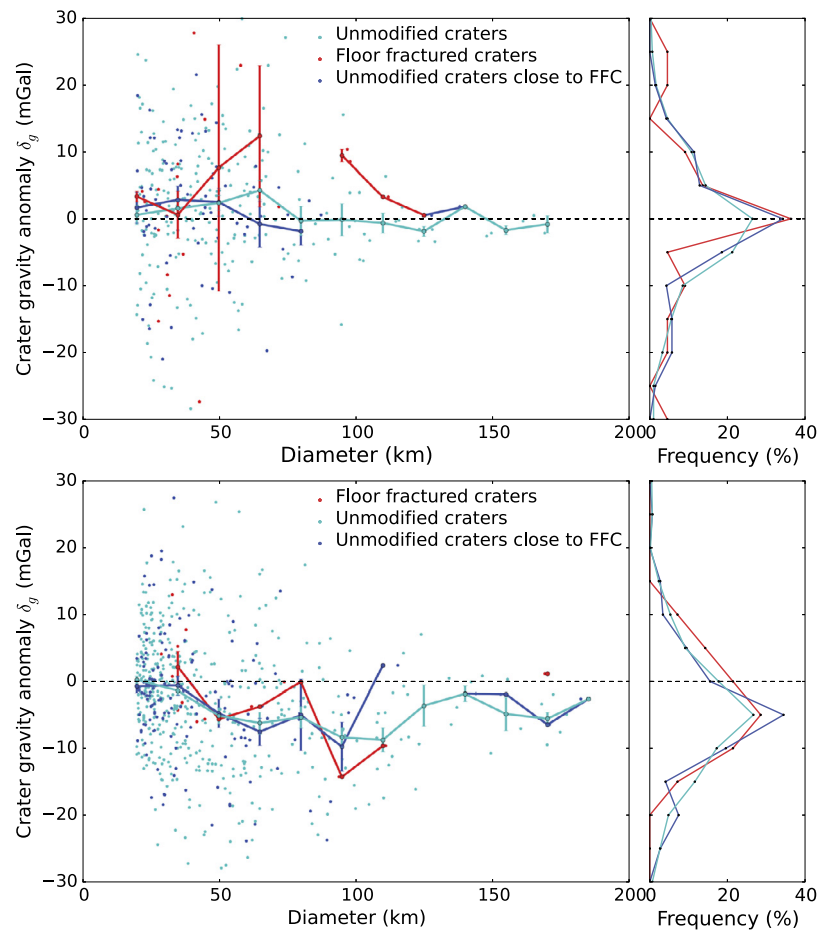
Fig. 8. (Top): Magnitude of the gravity anomaly δ_g versus diameter D for the normal crater population (light blue dots), the normal crater population that shares the FFC spatial distribution (blue dots) and the floor-fractured crater population (red dots) in the maria. Solid line: Mean of the gravity anomalies binned in 15 km diameter intervals. Error bars correspond to the standard error for each bin. Right plot: Corresponding gravity anomaly density distribution for each population in frequency (%). **(Bottom)**: Same plots but in South Pole–Aiken basin. (For interpretation of the references to color in this figure legend, the reader is referred to the web version of this article.)

measuring the FFC population mean ($\mu_{\delta_g} = 4.43 \pm 3.52$ mGal in the maria and $\mu_{\delta_g} = -0.25 \pm 2.52$ mGal in SPA).

4. Magmatic intrusion characteristics

Our results show that, on average, crustal gravity anomalies at floor-fractured craters are larger than at normal craters, but also that this result is statistically significant only for the highlands. This is in agreement with the presence of dense magmatic intrusions at depth below floor-fractured crater floors. In addition, the amplitudes of the gravitational signatures at floor-fractured craters are only of a few mGal, comparable to the predictions based on the theoretical model of Thorey and Michaut (2014) (Fig. 5). In the following, we compare the observed gravity signals at each floor-fractured crater to a synthetic gravity anomaly constructed based on the theoretical model of Thorey and Michaut (2014) in order to derive the mean density contrast between the intrusion and the surrounding crust. To that purpose, the thickness of each intrusion is needed and we use LOLA topographic data to estimate this quantity for each floor-fractured crater.

4.1. Intrusion thickness

The intrusion thickness H_0 at the center of the crater is taken as the amount of shallowing of the crater floor with respect to the expected depth (Schultz, 1976; Jozwiak et al., 2012). Given the observed crater depth, the problem is to estimate the orig-

inal crater depth before the intrusion formed. In the study of Jozwiak et al. (2012), the scaling law which gives the depth d_c as a function of the crater diameter D, derived by Pike (1974), was used as an estimate for the initial crater depth. However, this scaling law was calculated using only recent, Erastosthenian, and well preserved craters, and it is generally acknowledged that floor-fractured craters are generally older and more degraded than this population. In the absence of information on the state of degradation of lunar craters in the dataset of Head et al. (2010), we thus use the characteristics of the normal craters that share the spatial distribution of floor-fractured craters described in Section 3.1 as a reference.

We characterize the depths of both normal and floor-fractured craters using the 64 ppd (~450 m/pixel) LOLA gridded topography data (Zuber et al., 2009) obtained from the planetary data system geosciences node. We followed the method described by Kalynn et al. (2013) to derive the crater depth d_c and its uncertainty σ_d (see Supplementary Materials for details). Our d_c–D results for normal craters show trends that are consistent with previous works in the highlands, the lunar maria and the SPA (Fig. 9). Indeed, the crater depth of normal craters increases with increasing diameter and craters in the maria are on average shallower than in the highlands or SPA (Fig. 9) (Pike, 1974, 1980; Kalynn et al., 2013). Nevertheless, the variability in the degradation state of each crater results in an important variance in the crater depth with diameter with respect to the mean trend.
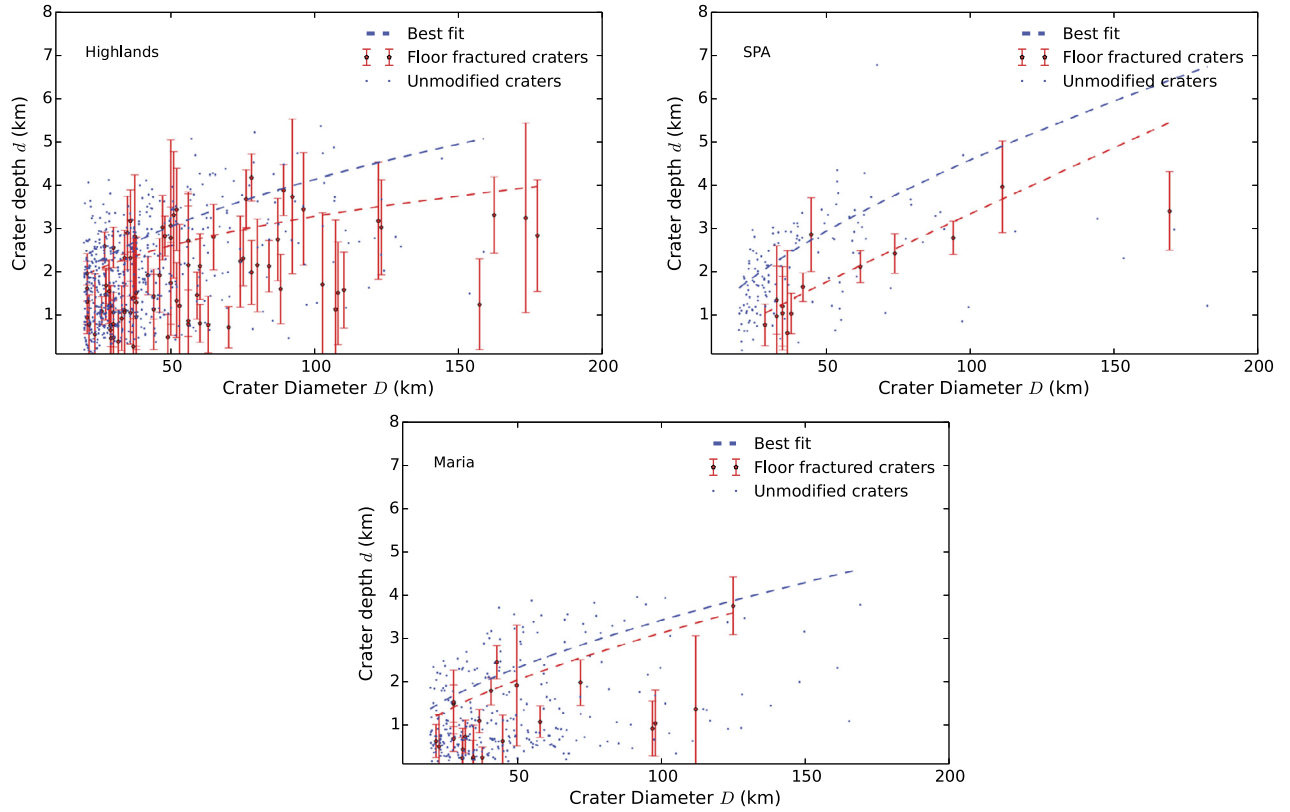
Fig. 9. Crater depth d_c (km) versus diameter D (km) for floor-fractured craters (red) and normal craters (blue) in the highlands, SPA and the maria. The normal craters in the highlands reference to the populations close to floor-fractured craters. Error bars are the uncertainties in the measurement of the crater depth and for clarity, the uncertainties are not shown for normal craters. Dashed lines: best fit using the equation $d_c = AD^B$ for the floor-fractured crater (red) and the normal crater (blue) populations in log–log space. Values of the coefficients A, B as well as the dispersion around the best fit line σ_{fit} are given in Supplementary Table 2. (For interpretation of the references to color in this figure legend, the reader is referred to the web version of this article.)

The same variability holds for the floor-fractured crater population depth (Fig. 9). This variability makes the identification of the uplift difficult at floor-fractured craters. Although the mean crater depth of floor-fractured craters in the highlands and SPA is slightly smaller than the mean of the normal crater population, the means of the two populations are not significantly different in the three regions (t-test: $p > 0.5$, Supplementary Table 2). A detailed geological study at each crater would be necessary to precisely identify the crater morphological structures and decrease the uncertainty in the depth estimation, but such a study is out of the scope of this article. We decided to estimate the intrusion thickness at floor-fractured craters only to a first order by considering the difference in the mean trends between normal and floor-fractured craters.

To characterize the mean trend of normal craters, we make use of a linear least-squares regression in log–log space to obtain a power law relationship of the form $d_c = AD^B$ (Pike, 1974; Kalynn et al., 2013). We use the same method to characterize the mean dependence of floor-fractured crater depth with crater diameter. In addition of determining the constant A and B, we also calculated the root-mean-squared dispersion σ_{fit} around the best fit (Supplementary Table 2). Subtracting the two best fit lines, we finally obtain a first-order estimate for the intrusion thickness at the center H_0 for each floor-fractured crater of given diameter D to which we assign an error $\sigma_{H_0} = (\sigma^2_{\text{fit-FFC}} + \sigma^2_{\text{fit-Unmod.Crater}})^{1/2}$.

4.2. Density contrast $\Delta\rho$ of the intrusion

We consider two different shapes for the intrusions beneath floor-fractured craters: a bell-shaped intrusion for craters that

show a convex floor (class 2 and 4 in the classification of Schultz, 1976) and a cylindrical-shaped intrusion for craters that show a plate-like floor (class 1, 3, 5 and 6 in the classification of Schultz, 1976). The two dimensionless profiles are described in Section 2.2 and each profile is redimensionalized using the thickness of the intrusion H_0 and its radius $D/2$ (see Section 4.1). The method used to derive the synthetic gravity anomaly from the intrusion thickness profile is detailed is Section 2.3. We use a unit density contrast, i.e. $\Delta\rho = 1$ kg m^{-3} and then filter the predicted gravity anomaly in exactly the same way than the observed gravity is filtered (Section 2.4). The synthetic gravity anomaly δ_g^s associated with each floor-fractured crater is defined as the mean of the synthetic gravity anomaly measured interior to the crater rim.

Finally, the density contrast between the magma and the crust at a specific floor-fractured crater location is given by the difference of the observed gravity anomaly δ_g^{obs} and the value of the gravity anomaly for normal craters δ_g^c of the same diameter, divided by the synthetic gravity anomaly for a unit density contrast δ_g^s

$$\Delta\rho = \frac{\delta_g^{obs} - \delta_g^c}{\delta_g^s} \tag{16}$$

where $\Delta\rho$ is in kg m^{-3}.

We find that the corrected gravity anomalies observed at floor-fractured crater sites in the highlands are consistent with a mean density contrast between the magma and the crust of $\mu_{\Delta\rho} = 913 \pm 269$ kg m^{-3} (Supplementary Table 4). In the maria, the corrected gravity anomalies observed in the 22 floor-fractured craters

are consistent with a mean density contrast equal to $\mu_{\Delta\rho} = 484 \pm 669$ kg m^{-3} (Supplementary Table 4). However, the difference between the mean density contrast in the highlands and the maria is not significant (a t-test gives a probability greater than 10% that this could occur by chance, $p > 0.1$). In the South Pole–Aikten basin, the corrected gravity anomalies observed in the 14 floor-fractured craters are consistent with a mean density contrast equal to $\mu_{\Delta\rho} = 974 \pm 846$ kg m^{-3} (Supplementary Table 4). But, the difference between the mean density contrast in the highlands and SPA is also not significant (a t test gives a probability greater than 50% that this could occur by chance, $p > 0.5$).

5. Discussion

In this study, we used the gravity field obtained by the GRAIL mission in combination with the topographic data obtained by the LOLA instrument to resolve mass anomalies below floor-fractured craters. We studied separately the craters in the farside highlands, South Pole–Aikten basin and maria to prevent potential bias from regional effects.

We show that the average gravitational signature of normal craters in the highlands is negative, whereas the average gravitational signature of floor-fractured craters is positive. Although a large variability characterizes the magnitude of gravity anomalies in both populations, the difference between the mean of the two populations, equal to $\sim$3 mGal, is statistically significant. In addition, the floor-fractured crater gravity anomalies do not follow the same dependence with diameter as normal craters. Our results are consistent with the emplacement of magmatic intrusions below floor-fractured craters as originally proposed by Schultz (1976). Furthermore, the observed gravity anomalies (after filtering) of a few mGal are in agreement with the values expected from the model of crater-centered intrusion of Thorey and Michaut (2014). In particular, measured gravity anomalies at floor-fractured craters imply an average density contrast between the magma and the surrounding crust equal to $\mu_{\Delta\rho} = 913 \pm 269$ kg m^{-3}. Thermal annealing could also participate to the measured gravity anomaly, which would then decrease the estimated density contrast, though this effect should be limited to a few percents (Michaut and Jaupart, 2011; Kiefer, 2013).

The grain density of lunar basalt can vary from 3270 kg m^{-3} for low Ti basalt to 3450 kg m^{-3} for high Ti basalt (Kiefer et al., 2012). In contrast, the lunar crust, which is mainly anorthositic, shows grain densities that vary from 2800 kg m^{-3} to 2900 kg m^{-3}. The grain density contrast between the magma and the crust should thus be between 370 and 650 kg m^{-3}, with an average of 510 kg m^{-3}. Impacts have induced fractures and created pore space in the lunar rocks decreasing their bulk densities. GRAIL data are consistent with an average porosity of about 12% in the crust (Wieczorek et al., 2013), and this porosity could be present in either, or both, of the two units (the surrounding crust and the magmatic intrusion).

First, the observed density contrast could be due to a pore-free magmatic intrusion and a pore free highland crust. From the sample densities, this would give rise to a density contrast of about 510 kg m^{-3}, which is smaller than the observed 1-σ lower bound, and thus is probably too small to account for the observations. Second, the density contrast could be the result of a fractured intrusion and a surrounding fractured highland crust. If each had the same level of porosity, this would give rise to an even smaller density contrast. Lastly, if the intrusion were unfractured, but the surrounding highland crust had a porosity of 12%, a density contrast of about 852 kg m^{-3} could be achieved, which is close to the observed value.

The best scenario that can account for the observed density contrast at floor-fractured craters in the highlands is an unfractured basaltic intrusion that forms within a fractured highland crust. Overall, this implies that the intrusion is sufficiently young to have escaped being fractured by subsequent impact events. Given that most basaltic eruptions occurred between 3 and 4 billion years ago, this suggests that the majority of the lunar crust was fractured before this date.

Our analyses of the gravity anomalies in the South Pole–Aikten basin and in the maria are less conclusive and are associated with much larger uncertainties. In regard to the SPA basin, although the mean magnitude of the gravity anomalies for floor-fractured craters is larger than for normal craters, we show that the difference between the two populations is not significant. We note, however, that the average density contrast associated with floor-fractured craters in the South Pole–Aitken basin is nearly identical to that obtained for the highlands.

Concerning the mare regions, the corrected gravity anomalies for floor-fractured craters are consistent with a mean value for the density contrast that is considerably smaller than in the highlands. This is in fact consistent with expectations. If the density contrast were the result of an unfractured intrusion forming in a fractured basaltic crust (both having the same grain density), the density contrast would be only about 403 kg m^{-3}, which is nearly identical to the mean value found from our analysis.

6. Conclusion

The gravitational signature of the floor-fractured crater population, first observed by Schultz (1976), has been investigated using the unprecedented resolution of the global gravity model provided by the GRAIL's mission. We show that the signal at floor-fractured craters in the highlands is consistent with the presence of a magmatic intrusion at depth below the crater floor. Derived synthetic gravity anomalies at each FFC compared to observations show that on average, the density contrast between the magma and the crust is about 913 kg m^{-3}. This value is in agreement with the intrusion being composed of unfractured basaltic material and forming in a pre-existing fractured crust (Wieczorek et al., 2013).

Similar studies have been carried out for floor-fractured craters located in the South Pole–Aikten basin and in the lunar maria. However, the small number of craters as well as the large variability in these two regions prevent from clearly differentiating the signal due to magmatic intrusions from the background. In general, two major questions need to be addressed before carrying out further investigations at floor-fractured crater sites: 1) What is the origin of the large variability in the magnitude of the gravity anomaly at normal craters? And 2), how can we better quantify the intrusion thickness at floor-fractured craters?

Indeed, our results suggest that the impact itself, combined with preexisting density variations within the crust, results in a wide range of Bouguer anomalies at normal impact craters. Such density structures should also preexist below floor-fractured craters before magma emplacement. To enhance the intrusion signal, an estimate of the expected initial gravity signature is desirable.

Additionally, we show that the large variability in the crater depth–diameter relationship makes difficult the determination of the crater depth itself, and by consequence, the thickness of the magmatic intrusion. This variability comes from the degradation state of the crater. A quantification of the degradation state of normal and floor-fractured craters might help to reduce the uncertainty in the determination of the initial and current floor-fractured crater depths and would result in a more accurate derivation of the density contrast between the magmatic intrusion and the surrounding crust.

Acknowledgements

Appendix A. Supplementary material

Supplementary material related to this article can be found online at http://dx.doi.org/10.1016/j.epsl.2015.04.021.

References

Andrews-Hanna, J.C., Asmar, S.W., Head, J.W., Kiefer, W.S., Konopliv, A.S., Lemoine, F.G., Matsuyama, I., Mazarico, E., McGovern, P.J., Melosh, H.J., Neumann, G.A., Nimmo, F., Phillips, R.J., Smith, D.E., Solomon, S.C., Taylor, G.J., Wieczorek, M.A., Williams, J.G., Zuber, M.T., 2013. Ancient igneous intrusions and early expansion of the Moon revealed by GRAIL gravity gradiometry. Science 339, 675–678. http://dx.doi.org/10.1126/science.1231753.

Besserer, J., Nimmo, F., Wieczorek, M.A., Weber, R.C., Kiefer, W.S., McGovern, P.J., Andrews-Hanna, J.C., Smith, D.E., Zuber, M.T., 2014. GRAIL gravity constraints on the vertical and lateral density structure of the lunar crust. Geophys. Res. Lett. 41, 1–7. http://dx.doi.org/10.1002/2014GL060240.

Dombard, A.J., Gillis, J.J., 2001. Testing the viability of topographic relaxation as a mechanism for the formation of lunar floor-fractured craters. J. Geophys. Res. 106, 27901–27909. http://dx.doi.org/10.1029/2000JE001388.

Garrick-Bethell, I., Zuber, M.T., 2009. Elliptical structure of the lunar South Pole–Aitken basin. Icarus 204, 399–408. http://dx.doi.org/10.1016/j.icarus.2009.05.032.

Hall, J.L., Solomon, S.C., Head, J.W., 1981. Lunar floor-fractured craters: evidence for viscous relaxation of crater topography. J. Geophys. Res., Planets 86, 9537–9552. http://dx.doi.org/10.1029/JB086iB10p09537.

Head, J.W., Fassett, C.I., Kadish, S.J., Smith, D.E., Zuber, M.T., Neumann, G.A., Mazarico, E., 2010. Global distribution of large lunar craters: implications for resurfacing and impactor populations. Science 329, 1504–1507. http://dx.doi.org/10.1126/science.1195050.

Huppert, H.E., 1982. The propagation of two-dimensional and axisymmetric viscous gravity currents over a rigid horizontal surface. J. Fluid Mech. 121, 43–58. http://dx.doi.org/10.1017/S0022112082001797.

Jozwiak, L.M., Head, J.W., Zuber, M.T., Smith, D.E., Neumann, G.A., 2012. Lunar floor-fractured craters: classification, distribution, origin and implications for magmatism and shallow crustal structure. J. Geophys. Res. 117, E11005. http://dx.doi.org/10.1029/2012JE004134.

Kalynn, J., Johnson, C.L., Osinski, G.R., Barnouin, O., 2013. Topographic characterization of lunar complex craters. Geophys. Res. Lett. 40, 38–42. http://dx.doi.org/10.1029/2012GL053608.

Kiefer, W.S., 2013. Gravity constraints on the subsurface structure of the Marius Hills: the magmatic plumbing of the largest lunar volcanic dome complex. J. Geophys. Res., Planets 118, 733–745. http://dx.doi.org/10.1029/2012JE004111.

Kiefer, W.S., Macke, R.J., Britt, D.T., Irving, A.J., Consolmagno, G.J., 2012. The density and porosity of lunar rocks. Geophys. Res. Lett. 39. http://dx.doi.org/10.1029/2012GL051319.

Konopliv, A.S., Park, R.S., Yuan, D.N., 2014. High-resolution lunar gravity fields from the GRAIL primary and extended missions. Geophys. Res. Lett. 41, 1452–1458. http://dx.doi.org/10.1002/2013GL059066.

Melosh, H.J., Freed, A.M., Johnson, B.C., Blair, D.M., Andrews-Hanna, J.C., Neumann, G.A., Phillips, R.J., Smith, D.E., Solomon, S.C., Wieczorek, M.A., Zuber, M.T., 2013. The origin of lunar mascon basins. Science 340, 1552–1555. http://dx.doi.org/10.1126/science.1235768.

Michaut, C., 2011. Dynamics of magmatic intrusions in the upper crust: theory and applications to laccoliths on Earth and the Moon. J. Geophys. Res. 116, B05205. http://dx.doi.org/10.1029/2010JB008108.

Michaut, C., Jaupart, C., 2011. Two models for the formation of magma reservoirs by small increments. Tectonophysics 500, 34–49. http://dx.doi.org/10.1016/j.tecto.2009.08.019.

Michaut, C., Baratoux, D., Thorey, C., 2013. Magmatic intrusions and deglaciation at mid-latitude in the northern plains of Mars. Icarus 225, 602–613. http://dx.doi.org/10.1016/j.icarus.2013.04.015.

Pike, R.J., 1974. Depth/diameter relations of fresh lunar craters: revision from spacecraft data. Geophys. Res. Lett. 1, 291–294. http://dx.doi.org/10.1029/GL001i007p00291.

Pike, R.J., 1980. Formation of complex impact craters: evidence from Mars and other planets. Icarus 43, 1–19. http://dx.doi.org/10.1016/0019-1035(80)90083-4.

Schultz, P.H., 1976. Floor-fractured lunar craters. The Moon 15, 241–273. http://dx.doi.org/10.1007/BF00562240.

Sjogren, W.L., Muller, P.M., Wollenhaupt, W.R., 1972. Apollo 15 gravity analysis from the S-band transponder experiment. The Moon 4, 411–418. http://dx.doi.org/10.1007/BF00562007.

Sjogren, W.L., Wimberly, R.N., Wollenhaupt, W.R., 1974. Lunar gravity: Apollo 16. The Moon 11, 35–40. http://dx.doi.org/10.1007/BF01877792.

Taisne, B., Tait, S., 2009. Eruption versus intrusion? Arrest of propagation of constant volume, buoyant, liquid-filled cracks in an elastic, brittle host. J. Geophys. Res. 114, B06202. http://dx.doi.org/10.1029/2009JB006297.

Thorey, C., Michaut, C., 2014. A model for the dynamics of crater-centered intrusion: application to lunar floor-fractured craters. J. Geophys. Res., Planets 119, 286–312. http://dx.doi.org/10.1002/2013je004467.

Walker, G.P.L., 1989. Gravitational (density) controls on volcanism, magma chambers and intrusions. Aust. J. Earth Sci. 36, 149–165. http://dx.doi.org/10.1080/08120098908729479.

Wichman, R.W., Schultz, P.H., 1995. Floor-fractured impact craters on Venus: implications for igneous crater modification and local magmatism. J. Geophys. Res. 100, 3233–3244. http://dx.doi.org/10.1029/94JE03206.

Wieczorek, M.A., Neumann, G.A., Nimmo, F., Kiefer, W.S., Taylor, G.J., Melosh, H.J., Phillips, R.J., Solomon, S.C., Andrews-Hanna, J.C., Asmar, S.W., Konopliv, A.S., Lemoine, F.G., Smith, D.E., Watkins, M.M., Williams, J.G., Zuber, M.T., 2013. The crust of the Moon as seen by GRAIL. Science 339, 671–675. http://dx.doi.org/10.1126/science.1231530.

Wieczorek, M.A., Phillips, R.J., 1998. Potential anomalies on a sphere: applications to the thickness of the lunar crust. J. Geophys. Res. 103, 1715–1724. http://dx.doi.org/10.1029/97JE03136.

Zuber, M.T., Smith, D.E., Watkins, M.M., Asmar, S.W., Konopliv, A.S., Lemoine, F.G., Melosh, H.J., Neumann, G.A., Phillips, R.J., Solomon, S.C., Wieczorek, M.A., Williams, J.G., Goossens, S.J., Kruizinga, G., Mazarico, E., Park, R.S., Yuan, D.N., 2013. Gravity field of the Moon from the gravity recovery and interior laboratory (GRAIL) mission. Science 339, 668–671. http://dx.doi.org/10.1126/science.1231507.

Zuber, M.T., Smith, D.E., Zellar, R.S., Neumann, G.A., Sun, X., Katz, R.B., Kleyner, I., Matuszeski, A., McGarry, J.F., Ott, M.N., Ramos-Izquierdo, L.A., Rowlands, D.D., Torrence, M.H., Zagwodzki, T.W., 2009. The lunar reconnaissance orbiter laser ranging Investigation. Space Sci. Rev. 150, 63–80. http://dx.doi.org/10.1007/s11214-009-9511-z.